

Chalcogenide Glass Microfibers for Mid-Infrared Optics

Dawei Cai ^{1,†}, Yu Xie ^{1,†}, Xin Guo ^{1,2}, Pan Wang ^{1,2} and Limin Tong ^{1,3,*}

¹ State Key Laboratory of Modern Optical Instrumentation, College of Optical Science and Engineering, Zhejiang University, Hangzhou 310027, China; caidawei@zju.edu.cn (D.C.); 11730034@zju.edu.cn (Y.X.); guoxin@zju.edu.cn (X.G.); nanopan@zju.edu.cn (P.W.)

² Intelligent Optics & Photonics Research Center, Jiaying Institute of Zhejiang University, Jiaying 314031, China

³ Collaborative Innovation Center of Extreme Optics, Shanxi University, Taiyuan 030006, China

* Correspondence: phytong@zju.edu.cn

† These authors contributed equally to this paper.

Abstract: With diameters close to the wavelength of the guided light, optical microfibers (MFs) can guide light with tight optical confinement, strong evanescent fields and manageable waveguide dispersion and have been widely investigated in the past decades for a variety of applications. Compared to silica MFs, which are ideal for working in visible and near-infrared regions, chalcogenide glass (ChG) MFs are promising for mid-infrared (mid-IR) optics, owing to their easy fabrication, broad-band transparency and high nonlinearity, and have been attracting increasing attention in applications ranging from near-field coupling and molecular sensing to nonlinear optics. Here, we review this emerging field, mainly based on its progress in the last decade. Starting from the high-temperature taper drawing technique for MF fabrication, we introduce basic mid-IR waveguiding properties of typical ChG MFs made of As₂S₃ and As₂Se₃. Then, we focus on ChG-MF-based passive optical devices, including optical couplers, resonators and gratings and active and nonlinear applications of ChG MFs for mid-IR Raman lasers, frequency combs and supercontinuum (SC) generation. MF-based spectroscopy and chemical/biological sensors are also introduced. Finally, we conclude the review with a brief summary and an outlook on future challenges and opportunities of ChG MFs.

Keywords: mid-infrared (mid-IR); chalcogenide glasses (ChGs); optical microfibers (MFs); supercontinuum (SC); molecular sensing



Citation: Cai, D.; Xie, Y.; Guo, X.; Wang, P.; Tong, L. Chalcogenide Glass Microfibers for Mid-Infrared Optics. *Photonics* **2021**, *8*, 497. <https://doi.org/10.3390/photonics8110497>

Received: 5 October 2021

Accepted: 3 November 2021

Published: 5 November 2021

Publisher's Note: MDPI stays neutral with regard to jurisdictional claims in published maps and institutional affiliations.



Copyright: © 2021 by the authors. Licensee MDPI, Basel, Switzerland. This article is an open access article distributed under the terms and conditions of the Creative Commons Attribution (CC BY) license (<https://creativecommons.org/licenses/by/4.0/>).

1. Introduction

In the past decades, optical microfibers (MFs) have brought wide opportunities in renewing and expanding fiber optics and technology at a wavelength scale [1–5]. Fabricated by a high-temperature taper-drawing technique [6], MFs exhibit excellent surface smoothness and diameter uniformity, which bestow them favorable features of low waveguiding loss [1,7], tight optical confinement, high fractional evanescent fields and large manageable waveguide dispersion [8], making them a versatile platform for both scientific research (e.g., optical nonlinearity [9–11] and atom optics [12–14]) and technological applications (e.g., optical sensors [15–17] and microlasers [18–20]). As one of the most widely studied optical materials, MFs based on silica have been employed for a variety of applications [3,4]; however, their uses in the mid-infrared (mid-IR, 2.5–20 μm) spectral range are restricted by strong absorption of silica glass [21]. In recent years, along with the rapid progress in mid-IR photonics, MFs for mid-IR photonics have attracted increasing interest [22,23].

Typically, mid-IR MFs are fabricated from a category of mid-IR-transparent materials, including oxide glasses (e.g., germanates [24], fluorotellurites [25] and tellurites [26]), fluoride glasses (ZBLAN) [27,28], chalcogenide glasses (ChGs, glasses containing one or more chalcogens: sulfur (S), selenium (Se) and tellurium (Te)) [29–31], as well as semiconductors (e.g., cadmium telluride (CdTe) and [32] silicon (Si) [33]). Among these materials, ChGs are mostly investigated for their special merits, including broadband intrinsic transparency

(0.5–25 μm), high optical nonlinearity (about 100–1000 times larger than that of silica glass) and hospitality to rare-earth dopants [29,34,35]. The typical optical loss of ChG fibers in the mid-IR is around 0.1–10 dB/m [35], while the lowest loss, down to 0.012 dB/m at 3 μm , has been reported in multimode As_2S_3 fibers [36]. Additionally, photonic devices based on ChG MFs, including resonators [37,38], gratings [39–41] and sensors [42,43], have been investigated in the visible (VIS) or near-infrared (near-IR) region and have recently extended to the mid-IR region [44–46]. In this review, combined with the latest progress in ChG MFs, we first introduce the fabrication and optical waveguiding properties of ChG MFs. Secondly, we introduce ChG MF-based passive optical devices (e.g., couplers, resonators and gratings), as well as active and nonlinear applications of ChG MFs in the mid-IR region including Raman lasers, frequency combs and supercontinuum (SC) generation, followed by MF-based spectroscopy and chemical/biological sensors. Finally, we summarize this review and present a brief outlook into future challenges and opportunities in this field.

2. Fabrication

Excellent surface smoothness and geometric uniformity are regarded as essential guarantees for achieving low-loss optical waveguiding in MFs. Typically, for MFs made of glass, the high-temperature taper-drawing process is the best technique for fabricating high-quality MFs with extremely low surface roughness (e.g., <0.5 nm [47]), excellent diameter uniformity and circular cross-section [48]. Tapered fibers based on mid-IR materials such as tellurite glass and fluorotellurite glass have been successfully fabricated [25,26]. Besides, owing to the relatively low softening temperature (T_s , e.g., 180 $^\circ\text{C}$ for As_2S_3 glass) of ChGs, ChG MFs are typically fabricated from ChG fibers heated by an electric heater (several millimeters in heating zone length) at a temperature slightly higher than the T_s [31,49], as schematically illustrated in Figure 1a. When stretching the fiber bi-directionally at both sides, the fiber is elongated and forms a waist (i.e., the MF) with two transition tapers connected to the untapered fibers. Close-up scanning electron microscope (SEM) images of an as-fabricated ChG (As_2S_3 glass) MF are shown in the inset of Figure 1a, showing the excellent surface smoothness and diameter uniformity.

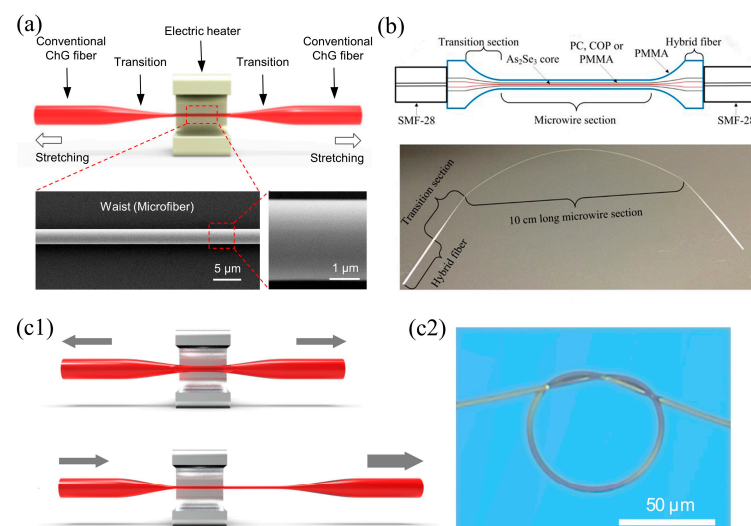


Figure 1. Fabrication of ChG MFs. (a) Schematic diagram of taper drawing a ChG MF from a conventional ChG fiber. Inset: SEM images of an as-fabricated As_2S_3 MF. (b) Schematic diagram of taper drawing a hybrid ChG-PMMA MF. Inset: optical image of as-fabricated hybrid ChG biconical fiber taper. Reprinted with the permission from [49] © The Optical Society. (c1) Schematic diagram of taper drawing a long-waist ChG MF by a two-step taper-drawing process. (c2) 62-micrometer diameter As_2S_3 MF-based knot assembled from a 3.5-micrometer diameter MF fabricated by the method in (c1). Reprinted with the permission from [45] © CLP Publishing.

Usually, made from soft glass, as-fabricated ChG MF is relatively fragile and easily damaged by mechanical disturbance. To enhance the mechanical strength of ChG MF and reduce its sensitivity to the surrounding environment, in 2010, Baker et al. reported a kind of hybrid ChG-PMMA fiber taper consisting of an As_2Se_3 core and a PMMA cladding [31]. The PMMA cladding possesses a T_s compatible with As_2Se_3 glass and enables taper-drawing fabrication of an MF from the two materials at the same time. A 9.7-cm-length hybrid biconical As_2Se_3 fiber taper with a core diameter down to 0.8 μm and a PMMA cladding diameter of 2.4 μm was fabricated successfully. In 2011, they demonstrated a generalized heat-brush tapering approach, which allowed the ratio of the feed and drawing velocities changes within each tapering sweep [50]. The waist diameter of the as-fabricated As_2Se_3 fiber taper decreased linearly from 15 to 10 μm over a 2.0-centimeter length. In 2016, Li et al. fabricated polymer-cladded (PC, COP or PMMA) As_2Se_3 fiber tapers with a waist diameter down to 1.5 μm and a waist length of 10 cm [49], as illustrated in Figure 1b. Both ends of the ChG fiber tapers were polished and adhered to single-mode silica fibers using UV-cured epoxy for efficient light input and output. Owing to the large waveguide nonlinear parameter and engineerable chromatic dispersion of the MFs, nonlinear optical effects including self-phase modulation, four-wave mixing and Raman scattering with wavelength up to 2.2 μm could be achieved.

To ease the tapering system and obtain long MFs with uniform diameters with a large reduction ratio of fiber diameter between the preform fiber and the final MF, in 2020, Xie et al. demonstrated a two-step taper-drawing process [45]. As schematically shown in Figure 1c1, commercial As_2S_3 fiber was first heated and stretched bi-directionally with a low speed ($0.4 \text{ mm}\cdot\text{s}^{-1}$). Secondly, the pre-drawn MF with a diameter in several micrometers was stretched unidirectionally at a fast rate ($6 \text{ mm}\cdot\text{s}^{-1}$) at one end and a slow rate ($0.4 \text{ mm}\cdot\text{s}^{-1}$) at the other end to draw a long-waist MF with a uniform diameter. Biconical fiber tapers with a waist length longer than 5 cm and diameters of around 3 μm were easily fabricated for assembling mid-IR photonic devices. In addition, as-drawn As_2S_3 MF (3.5- μm diameter) could be assembled into a 62- μm diameter knot structure with an elastic strain of up to 5.6% (Figure 1c2), indicating the excellent structural uniformity and surface-defect-free condition of the MF.

3. Optical Waveguiding Properties

MFs offer a number of attractive optical properties including tight optical confinement, strong evanescent field and tailorable waveguide dispersion [4,8]. The special merits of ChGs bestow the ChG MFs more possibilities. In this section, we discuss the optical properties of As_2S_3 (transmission range: 0.7–6 μm [35]) and As_2Se_3 (transmission range: 1–10 μm [35]) MFs contributed to applications such as optical waveguiding and nonlinearity. We assumed that the MF has a circular cross-section and an infinite air cladding with a step-index profile, and only the fundamental mode (HE_{11}) was considered. The refractive indices of the As_2S_3 (As_2Se_3) glass around 1.55- μm and 4- μm wavelengths are 2.44 (2.73) and 2.41 (2.68), respectively [51,52]. The refractive index of As_2Se_3 glass around 8- μm wavelength is 2.67.

The effective refractive index ($n_{\text{eff}} = \beta/k_0$, β is the propagation constant of the guided mode, $k_0 = 2\pi/\lambda$ is the wavenumber of the transmission wavelength λ), effective mode area (A_{eff}) and fractional evanescent fields (η) are essential waveguiding parameters for designing fiber-optic devices, including near-field couplers, gratings, resonators and sensors [31,53]. Figure 2a–c shows the calculated As_2S_3 and As_2Se_3 MF diameter-dependent n_{eff} , A_{eff} , and η in the mid-IR region, respectively. The results in the 1.55- μm wavelength (dash lines) are also shown for comparison. ChG MFs with diameters larger than the wavelengths of the guided light exhibit n_{eff} of HE_{11} mode close to the refractive indices of the bulk materials (Figure 2a), which is independent on the guided wavelength. When the diameter reduces close to or smaller than the wavelength, the n_{eff} decreases dramatically, indicating more fractional evanescent fields exist around the MF (Figure 2b), beneficial for enhancing interactions between the mid-IR light and samples surrounding the MF

in applications such as optical trapping, mid-IR spectroscopy and chemical/biological sensing related to molecular fingerprints [3,17,54]. Meanwhile, owing to the high nonlinear refractive index n_2 of As_2S_3 and As_2Se_3 materials and tight optical confinement (i.e., small A_{eff}) of the guided modes in MFs, these MFs usually have large effective nonlinearity γ ($\gamma = k_0 n_2 / A_{\text{eff}}$) and relatively low-threshold nonlinear optical effects when their diameters are close to the wavelength of the guided light in the material (i.e., λ/n , λ and n are the wavelength in air and refractive index of material, respectively). See Figure 2c) [31,55].

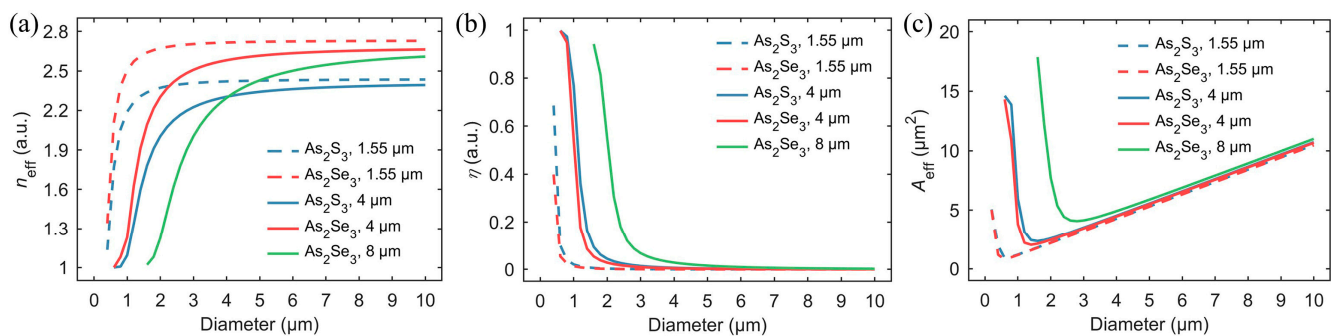


Figure 2. Numerical solutions of diameter-dependent (a) effective refractive index (n_{eff}), (b) fractional evanescent fields (η), and (c) effective mode area (A_{eff}) of As_2S_3 and As_2Se_3 MFs at wavelengths of 1.55 μm , 4 μm , and 8 μm , respectively.

4. Photonic Applications

4.1. Near-Field Optical Couplers

MF near-field couplers are simple fiber-optic components that can be used for efficient in/out-coupling with other optical structures such as micro/nano waveguides [48,56–58], whispering gallery mode (WGM) microcavities [59,60] and photonic crystal structures [61–63]. By precisely adjusting the coupling length or gap distance between the MF and the photonic structure, the phase-matching condition (and thus the coupling efficiency) can be precisely adjusted. MF near-field couplers possess the advantages of easy operation and small footprints.

With increasing demands of in/out coupler at mid-IR range in recent years, mid-IR MFs have been applied in the near-field optical coupling of a variety of photonic structures, including mid-IR waveguides and microcavities. For example, in 2018, to test the waveguiding properties of CdTe microwires (a quasi-one-dimensional single-crystal semiconductor) in the mid-IR region, Xin et al. used a 1.5- μm -diameter As_2S_3 MF as input coupler and a 5- μm -diameter As_2S_3 MF as output coupler for a 1.5- μm -diameter CdTe microwire (Figure 3a) [32]. The input MF diameter was carefully chosen to ensure single-mode operation within the 4.45–4.7 μm range. The relatively large effective refractive index contrast between the As_2S_3 MF and CdTe microwire can decrease the end-face reflection and achieve flat broadband coupling over the 4.45–4.7 μm and 8.36–8.6 μm range.

High-quality factor (Q , defined as the ratio of the resonant wavelength to the full width at half-maximum (FWHM)) resonators in the mid-IR are critical to promote the performances of mid-IR laser sources, cavity-based sensors and mid-IR frequency comb [66]. However, achieving ultra-high Q cavities and measuring their quality factors in the mid-IR remain challenging. In 2016, Lecaplain et al. developed an efficient coupling technique for WGM-based fluoride crystalline microresonators assisted by tapered ChG fibers (Figure 3b1) [64]. The ChG tapered fibers were pulled down to the 1- μm diameter (i.e., a ChG MF) to achieve phase matching with the fundamental WGMs of the resonator. By translating the microresonator along the taper relative to the waist, the phase-matching conditions were tuned precisely. Figure 3b2 shows the normalized transmission as a function of the coupling parameter. The data were consistent with the theoretical model ($K = \kappa_{\text{ex}} / \kappa_0 = (1 \pm \sqrt{T}) / (1 \mp \sqrt{T})$), in which κ_0 is the intrinsic loss rate, κ_{ex} is the coupling loss rate and T is the transmission). More recently, Xie et al. used As_2S_3 biconical tapered fibers for the first characterization of ChG microsphere resonators in the mid-IR re-

gion (Figure 3c) [65]. A 1.6- μm -diameter As_2S_3 fiber taper was used for near-field coupling with ChG microspheres with the coupling loss less than 3 dB over 4.465–4.705 μm .

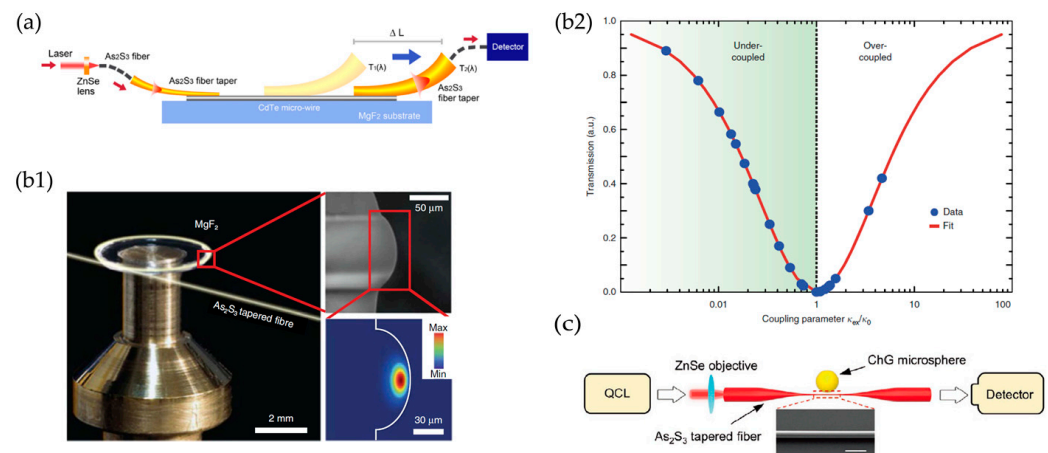


Figure 3. Mid-IR MF near-field couplers. (a) Schematic diagram of As_2S_3 tapered fiber coupler used for CdTe microwire transmission spectra measurement. Reprinted with the permission from [32] © The Optical Society. (b1) Optical micrograph and SEM image of the MgF_2 microresonator coupled with an As_2S_3 biconical fiber taper. Inset: Finite element model simulation of the optical intensity profile of the fundamental WGM at $\lambda = 4.5 \mu\text{m}$. (b2) Transmission as a function of the coupling parameter $K = \kappa_{ex} / \kappa_0$ for varying taper waist radius when taper-resonator coupling was achieved. Reprinted with the permission from [64] © Springer Nature. (c) Schematic illustration of As_2S_3 biconical fiber taper used for characterization of an As_2S_3 microsphere. Reprinted with the permission from [65] © John Wiley and Sons.

4.2. MF-Based Resonators

The combination of low-loss waveguiding and high-efficiency evanescent coupling between adjacent MFs bestows a kind of competitive high- Q resonators in various structures (e.g., loop [67,68], knot [1,69], ring [70–72] and coil [73,74]), showing the desirable features of easy fabrication, fiber compatibility and resonance tunability. During the past two decades, silica MF-based resonators have attracted wide attention in the VIS and near-IR applications, including optical filters, sensors and lasers [57,74–76]. Additionally, there are several kinds of high- Q (10^4 – 10^5) resonators based on ChG MFs in the near-IR region, including SU8 polymer-embedded As_2S_3 MF knot resonators (MKRs) (Figure 4a1,a2) [38], self-touching As_2Se_3 MF loop resonators (MLRs) by thermally shaping As_2Se_3 glass into an MF and splicing to cleaved silica fiber tapers (Figure 4b1,b2) [37] and resonators based on photoinduced WGMs localized in the cross-section of the ChG MFs [77]. These studies are beneficial to the further exploitations of ChGs, but they were not extended to the mid-IR region.

In 2020, Xie et al. demonstrated the first ChG MF-based resonator in the mid-IR region [45]. As_2S_3 MFs with uniform diameters and long waists were fabricated via a two-step taper drawing process (Figure 1c1). The MF structure was immersed in a drop of ethyl alcohol to avoid possible surface damage and assembled to a knot with double ends naturally connected to fiber tapers. Figure 4c1 shows an 824- μm diameter MKR assembled from a 3.2- μm -diameter As_2S_3 MF. A Q factor of about 2.84×10^4 was obtained at the wavelength of 4469.14 nm (Figure 4c2,c3). The free spectral range (FSR) of the MKR can not only be tuned by tightening the knot structure in liquid (Figure 4c4), but the resonance peaks can also be thermally tuned at a thermal tuning rate of $110 \text{ pm} \cdot ^\circ\text{C}^{-1}$ (Figure 4c5). Furthermore, to increase the long-term stability of the MKR device and isolate it from contaminations, a 551- μm -diameter MKR was embedded in low-index polymer (PMMA) film while a Q factor of 1.1×10^4 around 4.5- μm wavelength was retained.

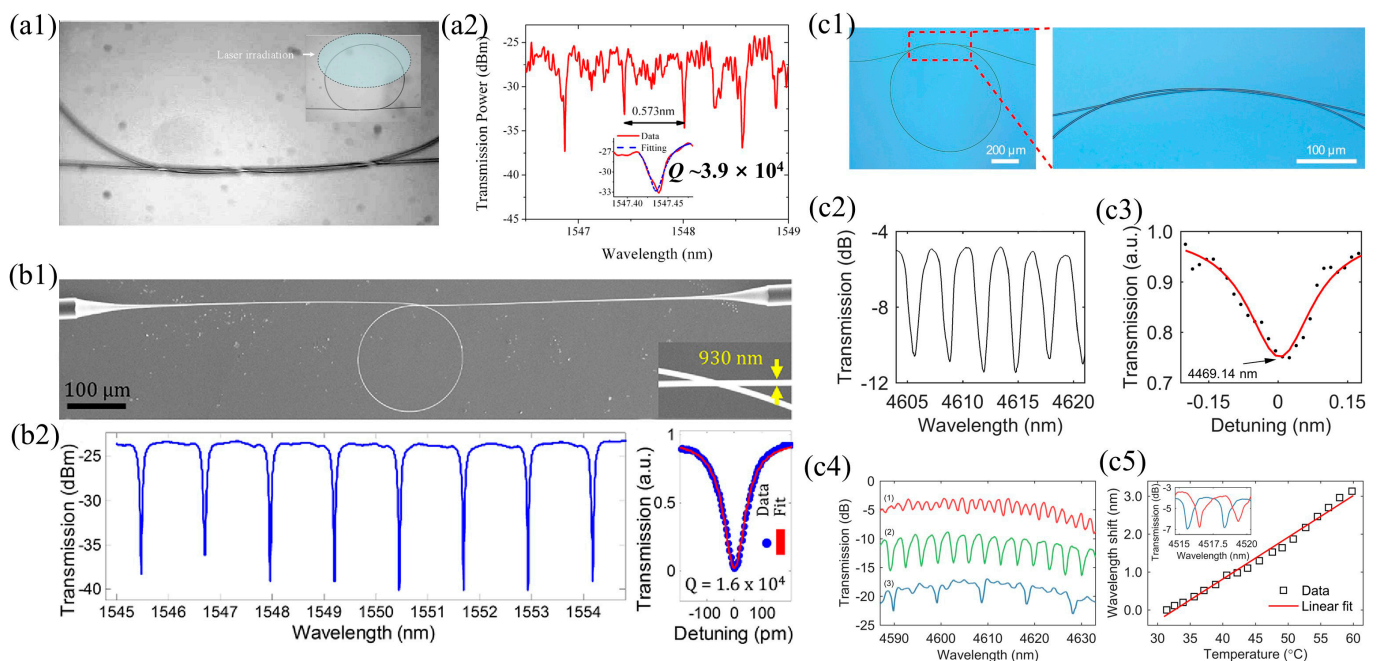


Figure 4. ChG MF-based resonators. (a1) Optical micrograph of the intertwined overlap region of a SU8 polymer-embedded As_2S_3 MKR. (a2) Transmission spectrum of the MKR. Reprinted with the permission from [38] © The Optical Society. (b1) SEM image of a 178.2- μm diameter As_2Se_3 MLR. The inset shows the self-coupling region. (b2) Transmission spectrum of the MLR. Inset: Lorentzian fitting to a resonance mode at 1552.9 nm. Reprinted with the permission from [37] © The Optical Society. (c1) Optical micrograph of an 824- μm diameter As_2S_3 MKR. Inset: optical micrograph of the intertwined overlap area. (c2) Transmission spectrum of the MKR. (c3) Lorentzian fitting to a resonance mode centered at 4469.14-nm wavelength. (c4) Transmission spectra of an As_2S_3 MKR by tightening the knot structure in liquid (from top to bottom). (c5) Resonance shift of an MKR with the temperature rising from 31.4 °C to 59.8 °C. Inset: transmission spectra of resonance modes corresponding to 31.4 °C (blue line) and 40.6 °C (red line). Reprinted with the permission from [45] © CLP Publishing.

As MF-based mid-IR resonators are essential for MF-based optical technology, they are expected to attract increasing attention in mid-IR optical applications, including mid-IR microlasers, narrow-wide filters, cavity-enhanced spectroscopy and the label-free detection of molecules [54,78].

4.3. MF Gratings

MF gratings have attracted intense attention owing to their miniaturized footprints, large fraction of evanescent field and high flexibility. Typical grating fabrication techniques include femtosecond (fs) laser inscription [79,80], ultraviolet laser irradiation [81] and focused ion beam milling [82,83]. So far, MF gratings have been employed for photonic sensors for measuring the refractive index, force and temperature, as well as for functionalized devices, including tunable filters and Fabry–Perot cavities [84–87].

Previously, ChG fiber gratings working in the mid-IR region [88] and ChG MF gratings working in the near-IR have been reported [40,89] (Figure 5a), while mid-IR MF gratings have been seldomly studied. In 2020, Cai et al. demonstrated the first mid-IR MF Bragg grating (mFBG) based on an As_2S_3 MF (Figure 5b1) [46]. The transmission spectrum shows a 15 dB depth around 4.5- μm wavelength (Figure 5b3), indicating a photo-induced refractive index change of 0.02. The dependence of the grating formation on the accumulated influence of exposure power density and time was also investigated. The interference pattern exposure technique can be applied to other photosensitive ChG MFs.

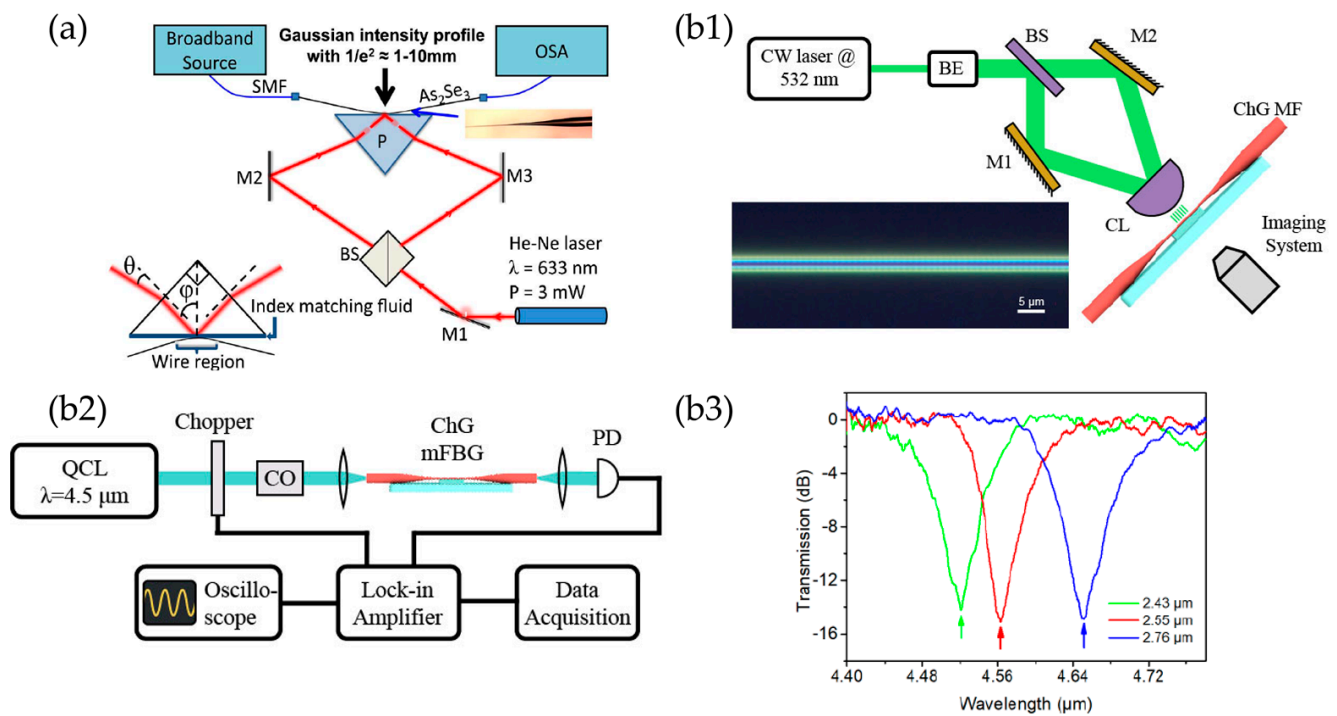


Figure 5. Mid-IR MF gratings. (a) Experimental setup for the As_2Se_3 MF Bragg grating photo inscription assisted by prism and in-situ monitoring of the process. Reprinted with the permission from [40] © The Optical Society. (b1) Schematic illustration of the As_2S_3 mFBG fabrication setup using interference pattern formed by two 532 nm beams. Inset: optical micrograph of a 2.4- μ m diameter ChG mFBG. (b2) Schematic illustration of the optical characterization of ChG mid-IR mFBGs. (b3) Transmission spectra of mFBGs with different MF diameters. Reprinted with the permission from [46] © The Optical Society.

Compared with conventional long-period grating (LPG), MFs could increase the depth of the evanescent field into the ambient environment, which may be helpful to enhance the performance of MF-based optical sensors. In 2019, Wang et al. reported a temperature sensor based on long-period fiber gratings (LPGs) inscribed on tapered multimode ChG fibers [90]. Simulation results show that the temperature sensitivity could be increased by reducing the waist diameter of tapered fiber. A resonant wavelength at 3 μ m was obtained when the period of LPGs was 176 μ m and the maximum sensitivity of temperature could achieve 12.6 nm/ $^{\circ}$ C at a 3-micrometer wavelength.

4.4. Raman Lasers

The Raman gain provided by silica fibers has led to Raman fiber lasers in the near-IR range for optical imaging and telecommunications-related applications [91]. The mid-IR Raman fiber lasers have been applied in LIDAR, pharmaceutical science and military applications [92,93]. The Raman gain coefficients of typical ChGs (e.g., $4.3\sim 5.7 \times 10^{-12}$ m/W for As_2S_3 and $2\sim 5 \times 10^{-11}$ m/W for As_2Se_3 at 1.5 μ m [94]) are more than 900 times larger than that of silica, making them excellent candidates for the mid-IR Raman lasers. In 2017, Abdukerim et al. demonstrated an all-fiber Raman laser based on a PMMA-coated 10-centimeter $As_{38}Se_{62}/As_{38}S_{62}$ MF [95]. The Raman laser emitted at 2.025 μ m with pump pulses at 1.938 μ m and a threshold pump power of 4.6 W (Figure 6a). To generate a shower of Raman solitons at the same wavelength, in 2021, Guo et al. pumped a 1960-nanometer picosecond laser into a tapered fluorotellurite MF and demonstrated Raman solitons around 3 μ m [96]. The group velocity dispersion was controlled by the diameter of the fluorotellurite MF, and all the generated solitons could be put at the same wavelength.

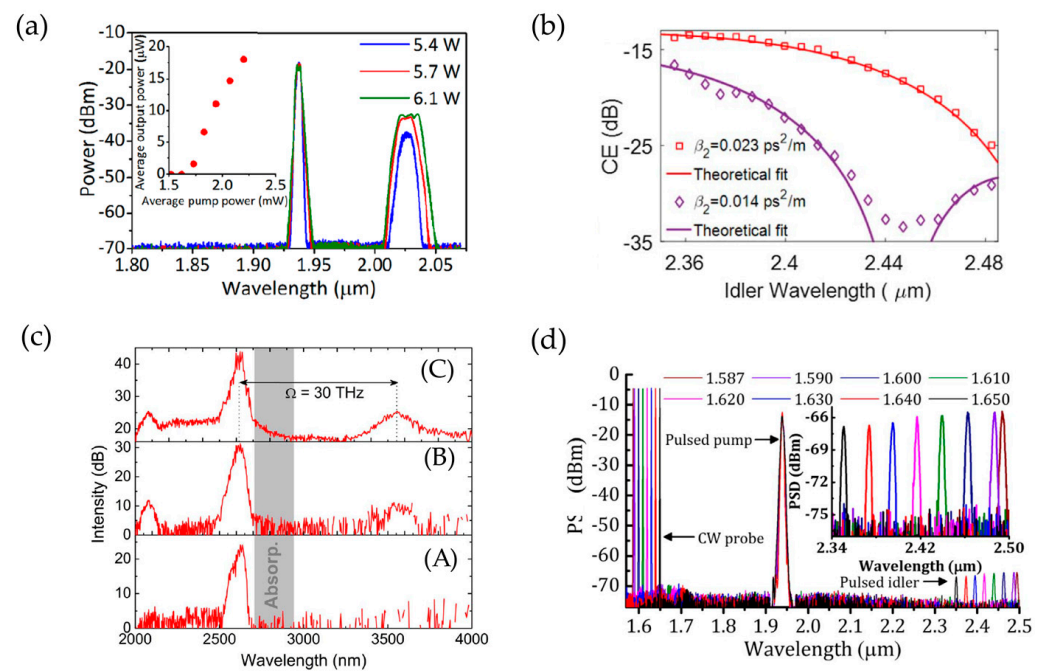


Figure 6. Raman scattering, four-wave mixing and modulation instability in mid-IR MFs. (a) Output spectra of the Raman laser based on a multi material ChG MF with increasing pump power. Inset: Average output power versus average pump power. Reprinted with the permission from [95] © AIP Publishing. (b) Conversion efficiency vs. idler wavelength for different tapering periods of all-fiber wavelength converters based on tapering As₂Se₃ MFs. Reprinted with the permission from [97] © The Optical Society. (c) Experimental observation of MI when pumping an As₂Se₃-polymer MF at $\lambda = 2620$ nm in the normal dispersion regime. Input peak powers estimated at (A) 200 mW, (B) 1 W and (C) 10 W. Reprinted with the permission from [98] © The Optical Society. (d) Measured output idler spectra resulting from wavelength tuning of the probe from 1.587 to 1.650 μm with a power of 0.54 mW. Reprinted with the permission from [99] © The Optical Society.

4.5. Frequency Conversion

Besides the large nonlinear optical coefficient and broad mid-IR transparency, ChGs are excellent candidates for mid-IR frequency conversion (e.g., optical parametric oscillation (OPO) and optical parametric amplification (OPA)) for their high laser damage threshold and moderate birefringence [100]. The efficiency of frequency conversion depends on phase matching, nonlinear gain and losses. The tapering of ChG fibers to increase nonlinearity while compensating the normal material dispersion has been demonstrated. In 2016, Abdukerim et al. reported the first fiber optical parametric oscillator (FOPO) using an As₂Se₃-COP MF at 2 μm based on four-wave mixing (FWM) [101]. The MF with a core diameter of 1.47 μm led to a waveguide nonlinearity of 24 $\text{W}^{-1}\text{m}^{-1}$ and a zero-dispersion wavelength of 1.875 μm . The FOPO had a pump threshold power of 5 W and covered a tunable wavelength range of 290 nm. In the FWM process, where pump and idler are far-detuned, the exact phase-matching wavelength is highly sensitive to chromatic dispersion and hard to control. In 2019, Alamgir et al. demonstrated the far-detuned wavelength converter by in-situ monitoring the output wavelength while tapering down the As₂Se₃ fiber [97]. As the tapering proceeded, the phase-matching condition was satisfied closer to the pump wavelength and the gain spectrum gradually shifted towards shorter wavelengths. The idlers were generated with a spectral range of 2.347–2.481 μm from a pump wavelength of 1.938 μm (Figure 6b).

The modulation instability (MI) is another frequency conversion process where the low-amplitude noise is parametrically amplified on the pump signal together with the growth of symmetric sidebands on both sides of the pump. Although most of the spontaneous MI requires pumping in the anomalous dispersion regime, MI can also be pumped

in a normal dispersion regime when the fiber possesses a higher-order group velocity dispersion profile. To prove the broadband frequency conversion due to normal dispersion MI, in 2014, Godin et al. demonstrated a parametric frequency conversion based on MI at 2 and 3.5 μm by pumping an As_2Se_3 -polymer MF with an fs OPO at 2.63 μm [98]. The measured frequency shift of 30 THz was the largest reported, using normal dispersion pumped MI in a single-pass configuration (Figure 6c). To prove the potential for improving the technical specifications of mid-IR fiber wavelength converter in terms of tunability and conversion efficiency, in 2017, Li et al. generated tunable parametric sidebands via MI in a 10-centimeter long As_2Se_3 -CYTOP tapered MF with a diameter of 1.625 μm (Figure 6d) [99]. The widely spaced Stokes and anti-Stokes bands were generated with a frequency shift as large as 49.3 THz, the largest reported in soft glass materials.

4.6. Supercontinuum Generation

Supercontinuum (SC) generation in optical fibers originates from the interaction between ultrashort laser pulses and fibers with high nonlinearity [107]. ChGs are regarded as good candidates for mid-IR SC generation with a large transparency window and comparatively high optical nonlinearity [22].

The uses of MFs reduce the power consumption and allow a shorter interaction length for SC generation. In 2013, Al-kadry et al. demonstrated SC generation from 1260 to 2200 nm using a 10-centimeter long As_2Se_3 MF [108]. The pump wavelength was self-frequency shifted to 1775 nm in the anomalous dispersion regime of the As_2Se_3 MF to avoid two photons' absorption. In the same year, Rudy et al. reported a generated SC from 1 to 3.7 μm in a 2.1-millimeter length As_2S_3 MF with 300-pJ 2-nanometer ultrafast pump pulses [109]. The spectral bandwidth was limited by the absorption caused by third harmonic generation. In 2014, Al-kadry et al. further used pump pulses of 800 fs at a 1.94- μm wavelength to generate an SC covered bandwidth of two octaves from 1.1 to 4.4 μm [102]. The waveguide nonlinearity of a 1.6-micrometer diameter As_2Se_3 MF was as high as $32.2 \text{ W}^{-1}\text{m}^{-1}$, resulting in a pumping power of only 500 pJ (Figure 7a). In 2017, Wang et al. investigated the dependence of the SC spectral behavior on the waist diameter and the transition region length of the tapered MF (Figure 7b) [103]. They reported a 1.4–7.2-micrometer SC generation with an average power of 1.06 mW from a 12-cm-length As-S tapered MF pumped at 3.25 μm .

Tapering the fiber is also an important method to obtain a highly coherent SC by designing an all-normal dispersion of fibers to suppress soliton effects including soliton fission and Raman soliton self-frequency shift. In 2019, Li et al. reported a 1.5–8.3 μm SC generation with a high coherence property from As-S tapered MF pumped at 3.75 μm (Figure 7c) [104]. They found that the coherence properties gradually become worse when the waist core diameters of tapered MFs decrease and a flat and near-zero dispersion is beneficial for high-coherence SC generation.

To meet the demanding specifications including robust and alignment-free sources of broadband SC, the multimaterial all-fiber-based SC systems have drawn much attention. In 2015, Sun et al. fabricated multimaterial As_2Se_3 - As_2S_3 ChG MFs with a zero-dispersion wavelength less than 2 μm [110]. The SC generation from 1.4 μm to longer than 4.8 μm was demonstrated by pumping the MF with 100 fs pulses at 3.4 μm . In 2017, Hudson et al. reported a 2.4 octave-SC generation by pumping a robust polymer-protected As_2Se_3 - As_2S_3 MF with 230 fs, 4.2 kW peak power pulses at 3 μm (Figure 7d) [105]. An average power spectral density of 0.003 mW/nm was achieved. Furthermore, significant power existed at various octave points throughout the SC, making the system a good candidate for an f - $2f$ interferometer.

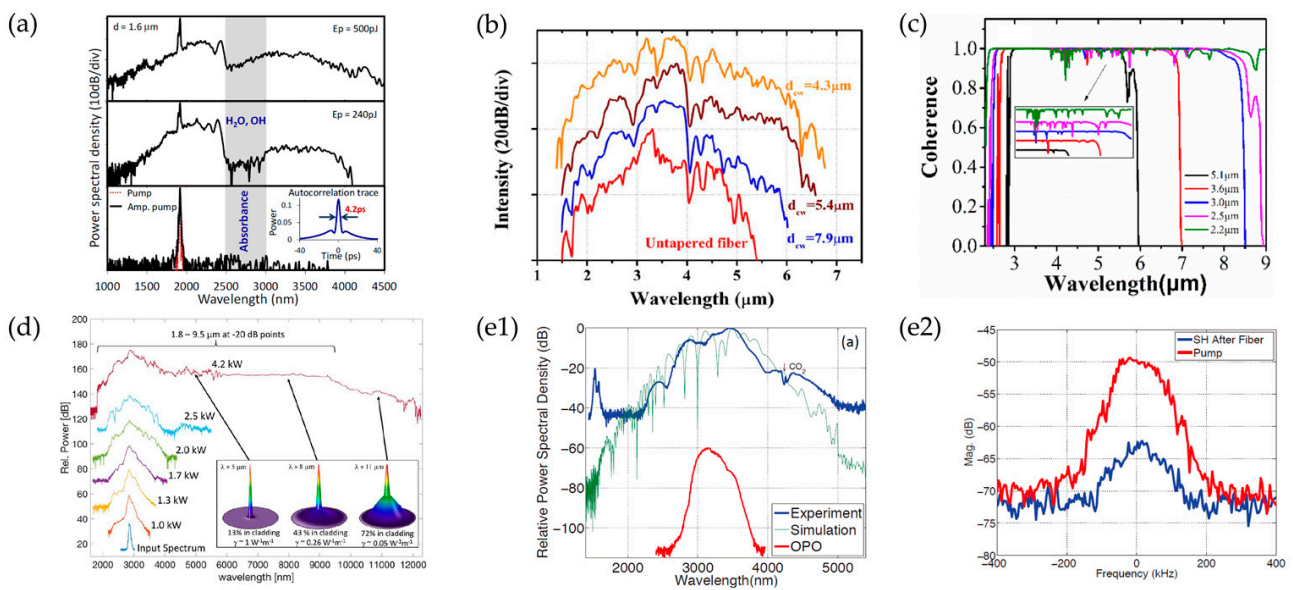


Figure 7. Supercontinuum generation and frequency comb generation in mid-IR MF. (a) SC spectra from amplified pump pulses using a 1.6-micrometer diameter As_2Se_3 MF for various amplified pump power levels. Inset: the autocorrelation trace of the amplified pump pulse. Reprinted with the permission from [102] © The Optical Society. (b) Measured SC spectra generated from 12-centimeter long As-S tapered MFs with diameters varying from 4.3 and 7.9 μm pumped at 3.25 μm . Reprinted with the permission from [103] © The Optical Society. (c) Simulated SC spectra coherence properties for different waist core diameters in As-S MFs. Reprinted with the permission from [104] © IEEE. (d) Spectral expansion at increasing peak power in a polymer-protected As_2Se_3/As_2S_3 MF pumping at 3 μm . The inset shows the mode profile in the MF section (3- μm core diameter) at various wavelengths. Reprinted with the permission from [105] © The Optical Society. (e1) Spectrum of SC generation around 3 μm from the As_2S_3 tapered MF compared with the OPO output and the simulation result (e2) RF spectrum of the interference of a c.w. laser at 1564 nm with the second harmonic (SH) of the tapered MF output. Reprinted with the permission from [106] © The Optical Society.

It is worth mentioning that another type of ChG MFs, tapered fibers with suspended-core geometry that operate in the anomalous dispersion regime, have been used to generate SC within a broad spectrum. In 2018, Anashkina et al. designed and developed $As_{39}Se_{61}$ suspended-core MFs for mid-IR SC generation. SC generation ranging from 1 to 10 μm was proposed with 150-fs 100-pJ pump pulses at 2 μm [111]. In 2020, Leonov et al. reported SC generation covering 1.4 to 4.2 μm in $As_{39}S_{61}$ suspended-core MFs pumped by a Cr:ZnSe laser. A maximum SC average power of ~ 35 mW was obtained with an optical efficiency of $\sim 35\%$ [112].

In addition, materials other than ChGs have also been investigated for SC generation. For example, compared to that of ChG, telluride glasses have shorter zero-dispersion wavelengths that are desirable for near-to-mid IR SC generation. In 2019, Saini et al. obtained an SC spectrum spanning 1.28–3.31 μm using a 3.2-centimeter-long tellurite tapered MF pumped with 200 fs laser pulse at 2.0 μm [26]. Compared to fluoride and chalcogenide fibers, fluorotellurite fibers based on $TeO_2-BaF_2-Y_2O_3$ have better chemical and thermal properties. In 2019, Li et al. demonstrated broadband SC generation from 0.6 to 5.4 μm in a fluorotellurite tapered MF pumped by a 2010 nm fs pulses [25]. Recently, polysilicon waveguides have emerged as an alternative platform as they are cheap and flexible to be incorporated into a wide range of geometries. In 2019, Ren et al. fabricated the tapered polycrystalline silicon core MFs (SCFs), and an SC spanning from 1.8 to 3.4 μm was obtained [33].

4.7. Frequency Combs

In the past years, frequency combs have been studied from the VIS and near-IR to the mid-IR regions. Mid-IR combs are of great use for molecular fingerprint spectroscopy

and are typically produced by OPOs [113,114], difference frequency generation [115,116], microresonators [117,118] and fs laser generation [119]. Wide frequency combs spectra in mid-IR have also been demonstrated using PPLN-based OPOs pumped by fiber-laser-based near-IR combs [120]. The mid-IR MFs could further broaden the frequency combs by SC generation when the generated SC maintains coherence with the pump laser. In 2012, Marandi et al. used a subharmonic OPO and subsequent SC generation in the tapered MF to convert the pulses of a conventional 1.5-micrometer frequency comb source to mid-IR [106]. The spectrum of the MF output extended from 2.2 to 5 μm at 40 dB below the peak (Figure 7e1). The beat frequencies in Figure 7e2 verified that the coherence properties of the initial frequency combs persevered. It is worth mentioning that, to simplify the mid-IR frequency comb generation, in 2014, Lee et al. demonstrated mid-IR frequency comb generation using a hybrid ChG-silica nanospine waveguide [121]. The waveguide was pumped directly by a two-micrometer frequency comb and could minimize the unwanted dispersion of pump pulses. The waveguide was small and simple using free-space coupling into and out of the fiber without an intermediate OPO.

4.8. MF-Based Sensors

The optical fiber sensors operating in the mid-IR region where the vibrational and rotational states of molecules are located play an important role in biomedical [122], chemical [123] and environmental applications [124].

The principle of fiber evanescent wave spectroscopy (FEWS) is based on the interaction between evanescent fields and chemical or biological specimens to be investigated, showing desirable advantages of analyzing samples in situ in real time. In past decades, many FEWS experiments have been applied in different areas including the detection of contaminants in water [128], metabolic profiling of chronic diseases [129] and monitoring of chemical processes [130]. The characterization of human tissue based on mid-IR FEWS is an important method for early and rapid diagnosis of diseases including tumors or cancers [131]. Typically, the fiber diameter used for FEWS is much larger than the working wavelength, leaving much space for sensitivity enhancement.

Owing to the characteristic fingerprints of a wide range of gases (e.g., CO, CO₂, NO and CH₄) falling in the mid-IR region, MF-based gas sensors have been proposed based on mid-IR absorption spectroscopy in the last decade [132]. In 2019, Huang et al. demonstrated a nonlinear gas sensor based on third harmonic generation (THG) in cascaded ChG MFs for detecting CH₄ (Figure 8a1) [125]. Mid-IR fingerprint light was absorbed in the first section of MF and the rest transmission signal was converted into a near-IR signal after THG at the second section. The proposed mid-IR ChG MF CH₄ sensor had a theoretical detection limit as low as 7.4×10^{-8} (Figure 8a2). Another configuration combines graphene with MFs, which can provide high-sensitivity optical gas sensing from permittivity change of the graphene. In 2019, Wang et al. reported a mid-IR gas sensor based on the graphene Bragg grating integrated with the Si slot MF (Figure 8b1) [126]. The NO₂ concentration could be determined from the 3 dB bandwidth of the Bragg grating's reflection band (Figure 8b2). A detection limit below 1 ppm and a sensitivity of 1.02 nm/ppm were achieved.

The optimization of the tapered transition structure of the fiber sensor is essential to obtain high-efficiency excitation of the evanescent fields to further enhance the sensor sensitivity. In 2021, Wang et al. reported a geometrical optimization of Ge-Sb-Se tapered MF for concentration sensing of methanol (Figure 8c1,c2) [127]. The highest sensitivity of 0.0120 a.u./% was obtained from the MF with a down-taper transition length of 5.4 mm and an up-taper transition length of 7.9 mm. Meanwhile, Wang et al. from the same group investigated the dependence of the sensitivity (of aqueous ethanol solution) on the MF parameters (e.g., diameter and length) [133] and predicted that the sensitivity could be improved by decreasing the MF diameter and increasing the length of the taper waist.

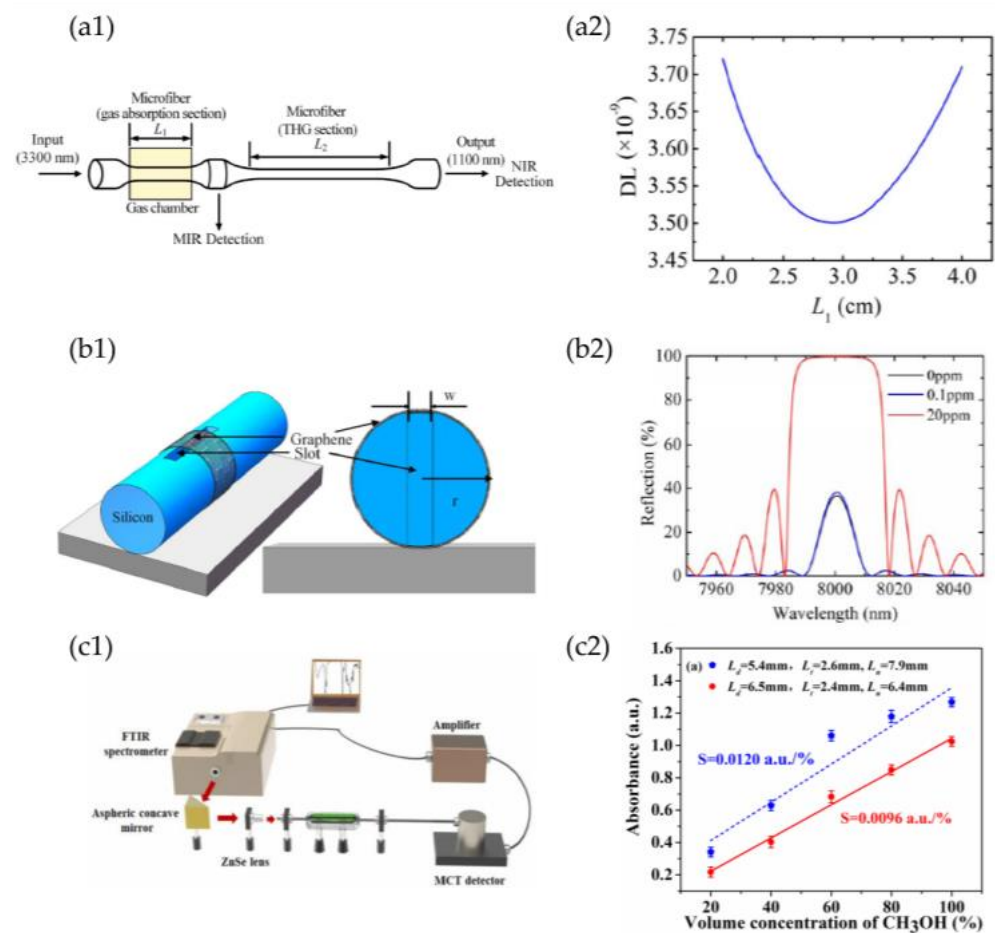


Figure 8. Mid-IR MF-based sensors. (a1) Schematic illustration of gas sensing based on cascaded ChG MFs. (a2) Detection limit of methane concentration for cascaded MFs sensing at different L_1 . Hereon, $L_2 = 9.5$ cm and $P_0 = 0.1$ W. Reprinted with the permission from [125] © The Optical Society. (b1) Schematic illustration of graphene on-Si slot fiber structure. (b2) Reflection spectra of Bragg gratings based on graphene on-Si slot fiber with different NO_2 gas concentrations. Reprinted with the permission from [126] © IEEE. (c1) Experimental setup of $\text{Ge}_{15}\text{Sb}_{15}\text{Se}_{70}$ tapered MF sensor. (c2) Dependence of the absorbance at $9.78 \mu\text{m}$ on the methanol aqueous solution concentration for the asymmetric and symmetric structure tapered fiber sensors. Reprinted with the permission from [127] © IEEE.

5. Discussion

In this article, a comprehensive survey of recent works on ChG MFs for the mid-IR range is presented, where the fabrication methods and the optical waveguiding properties (i.e., n_{eff} , A_{eff} and η) of ChG MFs are discussed. So far, high-quality ChG MFs (e.g., As_2S_3 and As_2Se_3 MFs) have been fabricated by a high-temperature taper drawing process and have shown great promise for broadband low-loss optical waveguiding in the mid-IR region. Based on these MFs, a new category of compact and fiber-compatible photonic devices has been developed for passive, active and nonlinear applications in the mid-IR region. These initial results have unambiguously suggested the great opportunities of using the ChG MF as a versatile platform for a miniaturized fiber-based platform for mid-IR optics.

6. Conclusions

Looking into the future, there are obvious challenges and opportunities for ChG MFs. First, compared with silica glass, ChGs possess a much higher refractive index and optical nonlinearity that are advantageous for tighter optical confinement and lower threshold for

nonlinear optical effects but exhibit much lower stability against optical, thermal, chemical and mechanical damages. Therefore, better package or protection techniques/protocols should be developed for real applications of ChG MFs, and more research efforts could be made on the material aspects. Secondly, compared to those for the VIS and near-IR spectral ranges, fiber-compatible devices for mid-IR, ranging from light sources, couplers, polarizers and filters to amplifiers, are typically not mature or optimized, leaving both challenges and opportunities in the future study of mid-IR MFs. Finally, other potentials, such as MF-incorporated plasmonic and atom optics that have been quite successful in the VIS/near-IR region, have not yet been equivalently investigated in mid-IR, which could be the new driving force in this field.

Author Contributions: Conceptualization, X.G., P.W. and L.T.; writing—original draft preparation, D.C. and Y.X.; writing—review and editing, D.C., Y.X., X.G., P.W. and L.T.; supervision, L.T.; project administration and funding acquisition, L.T. All authors have read and agreed to the published version of the manuscript.

Funding: This research was supported by the National Natural Science Foundation of China (11527901), Natural Science Foundation of Zhejiang Province (LR21F050002), and Fundamental Research Funds for the Central Universities.

Institutional Review Board Statement: Not applicable.

Informed Consent Statement: Not applicable.

Data Availability Statement: Not applicable.

Conflicts of Interest: The authors declare no conflict of interest.

References

1. Tong, L.M.; Gattass, R.R.; Ashcom, J.B.; He, S.L.; Lou, J.Y.; Shen, M.Y.; Maxwell, I.; Mazur, E. Subwavelength-diameter silica wires for low-loss optical wave guiding. *Nature* **2003**, *426*, 816–819. [[CrossRef](#)] [[PubMed](#)]
2. Brambilla, G.; Xu, F.; Horak, P.; Jung, Y.M.; Koizumi, F.; Sessions, N.P.; Koukharenko, E.; Feng, X.; Murugan, G.S.; Wilkinson, J.S.; et al. Optical fiber nanowires and microwires: Fabrication and applications. *Adv. Opt. Photonics* **2009**, *1*, 107–161. [[CrossRef](#)]
3. Tong, L.M.; Zi, F.; Guo, X.; Lou, J.Y. Optical microfibers and nanofibers: A tutorial. *Opt. Commun.* **2012**, *285*, 4641–4647. [[CrossRef](#)]
4. Wu, X.Q.; Tong, L.M. Optical microfibers and nanofibers. *Nanophotonics* **2013**, *2*, 407–428. [[CrossRef](#)]
5. Ismaeel, R.; Lee, T.; Ding, M.; Belal, M.; Brambilla, G. Optical microfiber passive components. *Laser Photonics Rev.* **2013**, *7*, 350–384. [[CrossRef](#)]
6. Ward, J.M.; O’Shea, D.G.; Shortt, B.J.; Morrissey, M.J.; Deasy, K.; Nic Chormaic, S.G. Heat-and-pull rig for fiber taper fabrication. *Rev. Sci. Instrum.* **2006**, *77*, 083105. [[CrossRef](#)]
7. Xu, Y.X.; Fang, W.; Tong, L.M. Real-time control of micro/nanofiber waist diameter with ultrahigh accuracy and precision. *Opt. Express* **2017**, *25*, 10434–10440. [[CrossRef](#)] [[PubMed](#)]
8. Tong, L.M.; Lou, J.Y.; Mazur, E. Single-mode guiding properties of subwavelength-diameter silica and silicon wire waveguides. *Opt. Express* **2004**, *12*, 1025–1035. [[CrossRef](#)] [[PubMed](#)]
9. Foster, M.A.; Moll, K.D.; Gaeta, A.L. Optimal waveguide dimensions for nonlinear interactions. *Opt. Express* **2004**, *12*, 2880–2887. [[CrossRef](#)]
10. Foster, M.A.; Turner, A.C.; Lipson, M.; Gaeta, A.L. Nonlinear optics in photonic nanowires. *Opt. Express* **2008**, *16*, 1300–1320. [[CrossRef](#)] [[PubMed](#)]
11. Leon-Saval, S.G.; Birks, T.A.; Wadsworth, W.J.; Russell, P.S.J.; Mason, M.W. Supercontinuum generation in submicron fibre waveguides. *Opt. Express* **2004**, *12*, 2864–2869. [[CrossRef](#)]
12. Balykin, V.I.; Hakuta, K.; Le Kien, F.; Liang, J.Q.; Morinaga, M. Atom trapping and guiding with a subwavelength-diameter optical fiber. *Phys. Rev. A* **2004**, *70*, 011401. [[CrossRef](#)]
13. Le Kien, F.; Balykin, V.I.; Hakuta, K. Atom trap and waveguide using a two-color evanescent light field around a subwavelength-diameter optical fiber. *Phys. Rev. A* **2004**, *70*, 063403. [[CrossRef](#)]
14. Sague, G.; Vetsch, E.; Alt, W.; Meschede, D.; Rauschenbeutel, A. Cold-atom physics using ultrathin optical fibers: Light-induced dipole forces and surface interactions. *Phys. Rev. Lett.* **2007**, *99*, 163602. [[CrossRef](#)] [[PubMed](#)]
15. Guo, X.; Ying, Y.B.; Tong, L.M. Photonic nanowires: From subwavelength waveguides to optical sensors. *Acc. Chem. Res.* **2014**, *47*, 656–666. [[CrossRef](#)] [[PubMed](#)]
16. Lou, J.Y.; Wang, Y.P.; Tong, L.M. Microfiber optical sensors: A review. *Sensors* **2014**, *14*, 5823–5844. [[CrossRef](#)] [[PubMed](#)]
17. Zhang, L.; Tang, Y.; Tong, L.M. Micro-/nanofiber optics: Merging photonics and material science on nanoscale for advanced sensing technology. *iScience* **2020**, *23*, 100810. [[CrossRef](#)] [[PubMed](#)]

18. Yang, Q.; Jiang, X.S.; Guo, X.; Chen, Y.; Tong, L.M. Hybrid structure laser based on semiconductor nanowires and a silica microfiber knot cavity. *Appl. Phys. Lett.* **2009**, *94*, 101108.
19. Jiang, X.S.; Song, Q.H.; Xu, L.; Fu, J.; Tong, L.M. Microfiber knot dye laser based on the evanescent-wave-coupled gain. *Appl. Phys. Lett.* **2007**, *90*, 233501. [[CrossRef](#)]
20. Jiang, X.S.; Yang, Q.; Vienne, G.; Li, Y.H.; Tong, L.M.; Zhang, J.J.; Hu, L.L. Demonstration of microfiber knot laser. *Appl. Phys. Lett.* **2006**, *89*, 143513. [[CrossRef](#)]
21. Nagel, S.R.; MacChesney, J.B.; Walker, K.L. *Optical Fiber Communications*, 1st ed.; Elsevier: New York, NY, USA, 1985; pp. 1–64.
22. Dai, S.X.; Wang, Y.Y.; Peng, X.F.; Zhang, P.Q.; Wang, X.S.; Xu, Y.S. A review of mid-Infrared supercontinuum generation in chalcogenide glass fibers. *Appl. Sci.* **2018**, *8*, 707. [[CrossRef](#)]
23. Gao, S.; Bao, X.Y. Chalcogenide taper and its nonlinear effects and sensing applications. *IScience* **2020**, *23*, 100802. [[CrossRef](#)] [[PubMed](#)]
24. Anashkina, E.A.; Andrianov, A.V.; Kim, A.V. Conversion of ultrashort laser pulses to wavelengths above 3 μm in tapered germanate fibres. *Quantum Electron.* **2015**, *45*, 437–442. [[CrossRef](#)]
25. Li, Z.R.; Yao, C.F.; Jia, Z.X.; Wang, F.; Qin, G.S.; Ohishi, Y.; Qin, W.P. Broadband supercontinuum generation from 600 to 5400 nm in a tapered fluorotellurite fiber pumped by a 2010 nm femtosecond fiber laser. *Appl. Phys. Lett.* **2019**, *115*, 091103. [[CrossRef](#)]
26. Saini, T.S.; Hoa, N.P.T.; Tuan, T.H.; Luo, X.; Suzuki, T.; Nish, Y. Tapered tellurite step-index optical fiber for coherent near-to-mid-IR supercontinuum generation: Experiment and modeling. *Appl. Opt.* **2019**, *58*, 415–421. [[CrossRef](#)] [[PubMed](#)]
27. Kubat, I.; Agger, C.S.; Moselund, P.M.; Bang, O. Mid-infrared supercontinuum generation to 45 μm in uniform and tapered ZBLAN step-index fibers by direct pumping at 1064 or 1550 nm. *J. Opt. Soc. Am. B* **2013**, *30*, 2743–2757. [[CrossRef](#)]
28. Chen, Z.G.; Taylor, A.J.; Efimov, A. Coherent mid-infrared broadband continuum generation in non-uniform ZBLAN fiber taper. *Opt. Express* **2009**, *17*, 5852–5860. [[CrossRef](#)] [[PubMed](#)]
29. Zakery, A.; Elliott, S.R. Optical properties and applications of chalcogenide glasses: A review. *J. Non-Cryst. Solids* **2003**, *330*, 1–12. [[CrossRef](#)]
30. Eggleton, B.J.; Luther-Davies, B.; Richardson, K. Chalcogenide photonics. *Nat. Photonics* **2011**, *5*, 141–148. [[CrossRef](#)]
31. Baker, C.; Rochette, M. Highly nonlinear hybrid AsSe-PMMA microtapers. *Opt. Express* **2010**, *18*, 12391–12398. [[CrossRef](#)]
32. Xin, C.G.; Wu, H.; Xie, Y.; Yu, S.L.; Zhou, N.; Shi, Z.X.; Guo, X.; Tong, L.M. CdTe microwires as mid-infrared optical waveguides. *Opt. Express* **2018**, *26*, 10944–10952. [[CrossRef](#)] [[PubMed](#)]
33. Ren, H.; Shen, L.; Wu, D.; Aktas, O.; Hawkins, T.; Ballato, J.; Gibson, U.J.; Peacock, A.C. Nonlinear optical properties of polycrystalline silicon core fibers from telecom wavelengths into the mid-infrared spectral region. *Opt. Mater. Express* **2019**, *9*, 1271–1279. [[CrossRef](#)]
34. Shiryaev, V.S.; Churbanov, M.F. Recent advances in preparation of high-purity chalcogenide glasses for mid-IR photonics. *J. Non-Cryst. Solids* **2017**, *475*, 1–9. [[CrossRef](#)]
35. Tao, G.M.; Ebendorff-Heidepriem, H.; Stolyarov, A.M.; Danto, S.; Badding, J.V.; Fink, Y.; Ballato, J.; Abouraddy, A.F. Infrared fibers. *Adv. Opt. Photonics* **2015**, *7*, 379–458. [[CrossRef](#)]
36. Churbanov, M.F.; Snopatin, G.E.; Shiryaev, V.S.; Plotnichenko, V.G.; Dianov, E.M. Recent advances in preparation of high-purity glasses based on arsenic chalcogenides for fiber optics. *J. Non-Cryst. Solids* **2011**, *357*, 2352–2357. [[CrossRef](#)]
37. Aktas, O. Chalcogenide microresonators tailored to distinct morphologies by the shaping of glasses on silica tapers. *Opt. Lett.* **2017**, *42*, 907–910. [[CrossRef](#)]
38. Zhang, Q.M.; Li, M.; Hao, Q.; Deng, D.H.; Zhou, H.; Zeng, H.P.; Zhan, L.; Wu, X.; Liu, L.Y.; Xu, L. Fabrication and characterization of on-chip optical nonlinear chalcogenide nanofiber devices. *Opt. Lett.* **2010**, *35*, 3829–3831. [[CrossRef](#)] [[PubMed](#)]
39. Ahmad, R.; Rochette, M. Photosensitivity at 1550 nm and Bragg grating inscription in As_2Se_3 chalcogenide microwires. *Appl. Phys. Lett.* **2011**, *99*, 061109. [[CrossRef](#)]
40. Ahmad, R.; Rochette, M.; Baker, C. Fabrication of Bragg gratings in subwavelength diameter As_2Se_3 chalcogenide wires. *Opt. Lett.* **2011**, *36*, 2886–2888. [[CrossRef](#)] [[PubMed](#)]
41. Florea, C.; Sanghera, J.S.; Shaw, B.; Aggarwal, I.D. Fiber Bragg gratings in As_2S_3 fibers obtained using a 0/−1 phase mask. *Opt. Mater.* **2009**, *31*, 942–944. [[CrossRef](#)]
42. Gao, S.; Baker, C.; Cai, W.; Chen, L.; Bao, X.Y. 10 kHz–34 MHz ultrasound detection based on a dual-core hybrid taper. *APL Photonics* **2019**, *4*, 110805. [[CrossRef](#)]
43. Fan, H.B.; Chen, L.; Bao, X.Y. Chalcogenide microfiber-assisted silica microfiber for ultrasound detection. *Opt. Lett.* **2020**, *45*, 1128–1131. [[CrossRef](#)] [[PubMed](#)]
44. Yeom, D.I.; Magi, E.C.; Lamont, M.R.; Roelens, M.A.; Fu, L.B.; Eggleton, B.J. Low-threshold supercontinuum generation in highly nonlinear chalcogenide nanowires. *Opt. Lett.* **2008**, *33*, 660–662. [[CrossRef](#)]
45. Xie, Y.; Cai, D.W.; Wu, H.; Pan, J.; Zhou, N.; Xin, C.G.; Yu, S.L.; Wang, P.; Jiang, X.S.; Qiu, J.R.; et al. Mid-infrared chalcogenide microfiber knot resonators. *Photonics Res.* **2020**, *8*, 616–621. [[CrossRef](#)]
46. Cai, D.W.; Xie, Y.; Wang, P.; Zhang, L.; Guo, X.; Tong, L.M. Mid-infrared microfiber Bragg gratings. *Opt. Lett.* **2020**, *45*, 6114–6117. [[CrossRef](#)] [[PubMed](#)]
47. Tong, L.M.; Lou, J.Y.; Ye, Z.Z.; Svacha, G.T.; Mazur, E. Self-modulated taper drawing of silica nanowires. *Nanotechnology* **2005**, *16*, 1445–1448. [[CrossRef](#)]

48. Tong, L.M.; Hu, L.L.; Zhang, J.J.; Qiu, J.R.; Yang, Q.; Lou, J.Y.; Shen, Y.H.; He, J.L.; Ye, Z.Z. Photonic nanowires directly drawn from bulk glasses. *Opt. Express* **2006**, *14*, 82–87. [[CrossRef](#)]
49. Li, L.Z.; Al-Kadry, A.; Abdurkerim, N.; Rochette, M. Design, fabrication and characterization of PC, COP and PMMA-cladded As_2Se_3 microwires. *Opt. Mater. Express* **2016**, *6*, 912–921. [[CrossRef](#)]
50. Baker, C.; Rochette, M. A generalized heat-brush approach for precise control of the waist profile in fiber tapers. *Opt. Mater. Express* **2011**, *1*, 1065–1076. [[CrossRef](#)]
51. Rodney, W.S.; Malitson, I.H.; King, T.A. Refractive index of arsenic trisulfide. *J. Opt. Soc. Am.* **1958**, *48*, 633–636. [[CrossRef](#)]
52. Van Popta, A.C.; DeCorby, R.G.; Haugen, C.J.; Robinson, T.; McMullin, J.N.; Tonchev, D.; Kasap, S.O. Photoinduced refractive index change in As_2Se_3 by 633 nm illumination. *Opt. Express* **2002**, *10*, 639–644. [[CrossRef](#)] [[PubMed](#)]
53. Huang, K.J.; Yang, S.Y.; Tong, L.M. Modeling of evanescent coupling between two parallel optical nanowires. *Appl. Opt.* **2007**, *46*, 1429–1434. [[CrossRef](#)]
54. Singh, V.; Lin, P.T.; Patel, N.; Lin, H.; Li, L.; Zou, Y.; Deng, F.; Ni, C.; Hu, J.; Giammarco, J.; et al. Mid-infrared materials and devices on a Si platform for optical sensing. *Sci. Technol. Adv. Mater.* **2014**, *15*, 014603. [[CrossRef](#)]
55. Hudson, D.D.; Dekker, S.A.; Maegi, E.C.; Judge, A.C.; Jackson, S.D.; Li, E.B.; Sanghera, J.S.; Shaw, L.B.; Aggarwal, I.D.; Eggleton, B.J. Octave spanning supercontinuum in an As_2S_3 taper using ultralow pump pulse energy. *Opt. Lett.* **2011**, *36*, 1122–1124. [[CrossRef](#)] [[PubMed](#)]
56. Guo, X.; Qiu, M.; Bao, J.M.; Wiley, B.J.; Yang, Q.; Zhang, X.N.; Ma, Y.G.; Yu, H.K.; Tong, L.M. Direct coupling of plasmonic and photonic nanowires for hybrid nanophotonic components and circuits. *Nano Lett.* **2009**, *9*, 4515–4519. [[CrossRef](#)] [[PubMed](#)]
57. Ding, Z.X.; Huang, Z.N.; Chen, Y.; Mou, C.B.; Lu, Y.Q.; Xu, F. All-fiber ultrafast laser generating gigahertz-rate pulses based on a hybrid plasmonic microfiber resonator. *Adv. Photon.* **2020**, *2*, 026002. [[CrossRef](#)]
58. Ma, Y.Q.; Farrell, G.; Semenova, Y.; Li, B.H.; Yuan, J.H.; Sang, X.Z.; Yan, B.B.; Yu, C.X.; Guo, T.; Wu, Q. Optical microfiber-loaded surface plasmonic TE-pass polarizer. *Opt. Laser Technol.* **2016**, *78*, 101–105. [[CrossRef](#)]
59. Vahala, K.J. Optical microcavities. *Nature* **2003**, *424*, 839–846. [[CrossRef](#)] [[PubMed](#)]
60. He, L.N.; Ozdemir, K.; Zhu, J.G.; Kim, W.; Yang, L. Detecting single viruses and nanoparticles using whispering gallery microlasers. *Nat. Nanotechnol.* **2011**, *6*, 428–432. [[CrossRef](#)]
61. Choi, J.; Noh, H. Enhanced absorption by coherent control in a photonic crystal resonator coupled with a microfiber. *Opt. Lett.* **2018**, *43*, 5532–5534. [[CrossRef](#)] [[PubMed](#)]
62. Kim, M.K.; Hwang, I.K.; Kim, S.H.; Chang, H.J.; Lee, Y.H. All-optical bistable switching in curved microfiber-coupled photonic crystal resonators. *Appl. Phys. Lett.* **2007**, *90*, 161118. [[CrossRef](#)]
63. Hwang, I.K.; Kim, S.K.; Yang, J.K.; Kim, S.H.; Lee, S.H.; Lee, Y.H. Curved-microfiber photon coupling for photonic crystal light emitter. *Appl. Phys. Lett.* **2005**, *87*, 131107. [[CrossRef](#)]
64. Lecaplain, C.; Javerzac-Galy, C.; Gorodetsky, M.L.; Kippenberg, T.J. Mid-infrared ultra-high-Q resonators based on fluoride crystalline materials. *Nat. Commun.* **2016**, *7*, 13383. [[CrossRef](#)] [[PubMed](#)]
65. Xie, Y.; Cai, D.W.; Pan, J.; Zhou, N.; Gao, Y.X.; Jin, Y.Y.; Jiang, X.S.; Qiu, J.R.; Wang, P.; Guo, X.; et al. Batch fabrication of high-quality infrared chalcogenide microsphere resonators. *Small* **2021**, *17*, 2100140. [[CrossRef](#)] [[PubMed](#)]
66. Heylman, K.D.; Knapper, K.A.; Horak, E.H.; Rea, M.T.; Vanga, S.K.; Goldsmith, R.H. Optical microresonators for sensing and transduction: A materials perspective. *Adv. Mater.* **2017**, *29*, 1700037. [[CrossRef](#)]
67. Sumetsky, M.; Dulashko, Y.; Fini, J.M.; Hale, A.; DiGiovanni, D.J. The microfiber loop resonator: Theory, experiment, and application. *J. Lightwave Technol.* **2006**, *24*, 242–250. [[CrossRef](#)]
68. Guo, X.; Li, Y.H.; Jiang, X.S.; Tong, L.M. Demonstration of critical coupling in microfiber loops wrapped around a copper rod. *Appl. Phys. Lett.* **2007**, *91*, 073512. [[CrossRef](#)]
69. Jiang, X.S.; Tong, L.M.; Vienne, G.; Guo, X.; Tsao, A.; Yang, Q.; Yang, D.R. Demonstration of optical microfiber knot resonators. *Appl. Phys. Lett.* **2006**, *88*, 223501. [[CrossRef](#)]
70. Wang, P.; Zhang, L.; Yang, Z.Y.; Gu, F.X.; Wang, S.S.; Yang, Q.; Tong, L.M. Fusion spliced microfiber closed-loop resonators. *IEEE Photonics Technol. Lett.* **2010**, *22*, 1075–1077. [[CrossRef](#)]
71. Li, W.; Wang, P.; Hu, Z.F.; Tong, L.M. Fusion splicing soft glass microfibers for photonic devices. *IEEE Photonics Technol. Lett.* **2011**, *23*, 831–833. [[CrossRef](#)]
72. Zhang, B.; Zeng, P.Y.; Yang, Z.L.; Xia, D.; Zhao, J.X.; Sun, Y.D.; Huang, Y.F.; Song, J.C.; Pan, J.S.; Cheng, H.J.; et al. On-chip chalcogenide microresonators with low-threshold parametric oscillation. *Photonics Res.* **2021**, *9*, 1272–1279. [[CrossRef](#)]
73. Sumetsky, M. Optical fiber microcoil resonators. *Opt. Express* **2004**, *12*, 2303–2316. [[CrossRef](#)]
74. Scheuer, J.; Sumetsky, M. Optical-fiber microcoil waveguides and resonators and their applications for interferometry and sensing. *Laser Photon. Rev.* **2011**, *5*, 465–478. [[CrossRef](#)]
75. Xu, Z.L.; Sun, Q.Z.; Li, B.R.; Luo, Y.Y.; Lu, W.G.; Liu, D.M.; Shum, P.P.; Zhang, L. Highly sensitive refractive index sensor based on cascaded microfiber knots with Vernier effect. *Opt. Express* **2015**, *23*, 6662–6672. [[CrossRef](#)] [[PubMed](#)]
76. Liu, M.; Tang, R.; Luo, A.P.; Xu, W.C.; Luo, Z.C. Graphene-decorated microfiber knot as a broadband resonator for ultrahigh-repetition-rate pulse fiber lasers. *Photonics Res.* **2018**, *6*, C1–C7. [[CrossRef](#)]
77. Luan, F.; Magi, E.; Gong, T.X.; Kabakova, I.; Eggleton, B.J. Photoinduced whispering gallery mode microcavity resonator in a chalcogenide microfiber. *Opt. Lett.* **2011**, *36*, 4761–4763. [[CrossRef](#)] [[PubMed](#)]

78. Ma, P.; Choi, D.Y.; Yu, Y.; Yang, Z.Y.; Vu, K.; Nguyen, T.; Mitchell, A.; Luther-Davies, B.; Madden, S. High Q factor chalcogenide ring resonators for cavity-enhanced MIR spectroscopic sensing. *Opt. Express* **2015**, *23*, 19969–19979. [[CrossRef](#)] [[PubMed](#)]
79. Grobncic, D.; Mihailov, S.J.; Ding, H.M.; Smelser, C.W. Bragg grating evanescent field sensor made in biconical tapered fiber with femtosecond IR radiation. *IEEE Photonics Technol. Lett.* **2006**, *18*, 160–162. [[CrossRef](#)]
80. Fang, X.; Liao, C.R.; Wang, D.N. Femtosecond laser fabricated fiber Bragg grating in microfiber for refractive index sensing. *Opt. Lett.* **2010**, *35*, 1007–1009. [[CrossRef](#)]
81. Ran, Y.; Jin, L.; Tan, Y.N.; Sun, L.P.; Li, J.; Guan, B.O. High-efficiency ultraviolet inscription of Bragg gratings in microfibers. *IEEE Photonics J.* **2012**, *4*, 181–186. [[CrossRef](#)]
82. Kou, J.L.; Qiu, S.J.; Xu, F.; Lu, Y.Q. Demonstration of a compact temperature sensor based on first-order Bragg grating in a tapered fiber probe. *Opt. Express* **2011**, *19*, 18452–18457. [[CrossRef](#)] [[PubMed](#)]
83. Liu, Y.X.; Meng, C.; Zhang, A.P.; Xiao, Y.; Yu, H.K.; Tong, L.M. Compact microfiber Bragg gratings with high-index contrast. *Opt. Lett.* **2011**, *36*, 3115–3117. [[CrossRef](#)] [[PubMed](#)]
84. Nayak, K.P.; Le Kien, F.; Kawai, Y.; Hakuta, K.; Nakajima, K.; Miyazaki, H.T.; Sugimoto, Y. Cavity formation on an optical nanofiber using focused ion beam milling technique. *Opt. Express* **2011**, *19*, 14040–14050. [[CrossRef](#)] [[PubMed](#)]
85. Guan, B.O.; Li, J.; Jin, L.; Ran, Y. Fiber Bragg gratings in optical microfibers. *Opt. Fiber Technol.* **2013**, *19*, 793–801. [[CrossRef](#)]
86. Gao, S.; Jin, L.; Ran, Y.; Sun, L.P.; Li, J.; Guan, B.O. Temperature compensated microfiber Bragg gratings. *Opt. Express* **2012**, *20*, 18281–18286. [[CrossRef](#)] [[PubMed](#)]
87. Luo, W.; Kou, J.L.; Chen, Y.; Xu, F.; Lu, Y.Q. Ultra-highly sensitive surface-corrugated microfiber Bragg grating force sensor. *Appl. Phys. Lett.* **2012**, *101*, 133502. [[CrossRef](#)]
88. Bernier, M.; El-Amraoui, M.; Couillard, J.F.; Messaddeq, Y.; Vallee, R. Writing of Bragg gratings through the polymer jacket of low-loss As₂S₃ fibers using femtosecond pulses at 800 nm. *Opt. Lett.* **2012**, *37*, 3900–3902. [[CrossRef](#)] [[PubMed](#)]
89. Baker, C.; Gao, S.; Chen, L.; Bao, X.Y. Self-inscribed antisymmetric long-period grating in a dual-core As₂Se₃-PMMA fiber. *Opt. Express* **2017**, *25*, 12409–12414. [[CrossRef](#)]
90. Wang, L.L.; Ma, W.Q.; Zhang, P.Q.; Yang, D.D.; Zhu, L.; Wang, X.S.; Dai, S.X. Design and analysis of long-period fiber gratings in tapered multimode chalcogenide glass fiber for temperature measurement. *J. Opt. Soc. Am. B* **2019**, *36*, 1792–1798. [[CrossRef](#)]
91. Supradeepa, V.R.; Feng, Y.; Nicholson, J.W. Raman fiber lasers. *J. Opt.* **2017**, *19*, 023001. [[CrossRef](#)]
92. Pierce, M.C.; Jackson, S.D.; Dickinson, M.R.; King, T.A.; Sloan, P. Laser-tissue interaction with a continuous wave 3- μ m fibre laser: Preliminary studies with soft tissue. *Lasers Surg. Med.* **2000**, *26*, 491–495. [[CrossRef](#)]
93. Jackson, S.D. Towards high-power mid-infrared emission from a fibre laser. *Nat. Photonics* **2012**, *6*, 423–431. [[CrossRef](#)]
94. White, R.T.; Monro, T.M. Cascaded Raman shifting of high-peak-power nanosecond pulses in As₂S₃ and As₂Se₃ optical fibers. *Opt. Lett.* **2011**, *36*, 2351–2353. [[CrossRef](#)] [[PubMed](#)]
95. Abdukerim, N.; Li, L.Z.; El Amraoui, M.; Messaddeq, Y.; Rochette, M. 2 μ m Raman fiber laser based on a multimaterial chalcogenide microwire. *Appl. Phys. Lett.* **2017**, *110*, 161103. [[CrossRef](#)]
96. Guo, X.H.; Li, Z.R.; Jiao, Y.D.; Zhao, Z.P.; Yao, C.F.; Jia, Z.X.; Dong, K.G.; Zhang, H.Y.; Lin, H.H.; Qin, W.P.; et al. A shower of mid-infrared Raman solitons at designed wavelength of similar to 3 μ m from a tapered fluorotellurite fiber. *Laser Phys.* **2021**, *31*, 095103. [[CrossRef](#)]
97. Alamgir, I.; Abdukerim, N.; Rochette, M. In situ fabrication of far-detuned optical fiber wavelength converters. *Opt. Lett.* **2019**, *44*, 4467–4470. [[CrossRef](#)] [[PubMed](#)]
98. Godin, T.; Combes, Y.; Ahmad, R.; Rochette, M.; Sylvestre, T.; Dudley, J.M. Far-detuned mid-infrared frequency conversion via normal dispersion modulation instability in chalcogenide microwires. *Opt. Lett.* **2014**, *39*, 1885–1888. [[CrossRef](#)] [[PubMed](#)]
99. Li, L.Z.; Abdukerim, N.; Rochette, M. Mid-infrared wavelength conversion from As₂Se₃ microwires. *Opt. Lett.* **2017**, *42*, 639–642. [[CrossRef](#)]
100. Liang, F.; Kang, L.; Lin, Z.S.; Wu, Y.C. Mid-infrared nonlinear optical materials based on metal chalcogenides: Structure-property relationship. *Cryst. Growth Des.* **2017**, *17*, 2254–2289. [[CrossRef](#)]
101. Abdukerim, N.; Li, L.Z.; Rochette, M. Chalcogenide-based optical parametric oscillator at 2 μ m. *Opt. Lett.* **2016**, *41*, 4364–4367. [[CrossRef](#)]
102. Al-Kadry, A.; El Amraoui, M.; Messaddeq, Y.; Rochette, M. Two octaves mid-infrared supercontinuum generation in As₂Se₃ microwires. *Opt. Express* **2014**, *22*, 31131–31137. [[CrossRef](#)] [[PubMed](#)]
103. Wang, Y.Y.; Dai, S.X.; Li, G.T.; Xu, D.; You, C.Y.; Han, X.; Zhang, P.Q.; Wang, X.S.; Xu, P.P. 1.4–7.2 μ m broadband supercontinuum generation in an As-S chalcogenide tapered fiber pumped in the normal dispersion regime. *Opt. Lett.* **2017**, *42*, 3458–3461. [[CrossRef](#)] [[PubMed](#)]
104. Li, G.T.; Peng, X.F.; Dai, S.X.; Wang, Y.Y.; Xie, M.; Yang, L.; Yang, C.F.; Wei, W.Y.; Zhang, P.Q. Highly coherent 1.5–8.3 μ m broadband supercontinuum generation in tapered As-S chalcogenide fibers. *J. Lightwave Technol.* **2019**, *37*, 1847–1852. [[CrossRef](#)]
105. Hudson, D.D.; Antipov, S.; Li, L.Z.; Alamgir, I.; Hu, T.; Amraoui, M.; Messaddeq, Y.; Rochette, M.; Jackson, S.D.; Fuerbach, A. Toward all-fiber supercontinuum spanning the mid-infrared. *Optica* **2017**, *4*, 1163–1166. [[CrossRef](#)]
106. Marandi, A.; Rudy, C.W.; Plotnichenko, V.G.; Dianov, E.M.; Vodopyanov, K.L.; Byer, R.L. Mid-infrared supercontinuum generation in tapered chalcogenide fiber for producing octave-spanning frequency comb around 3 μ m. *Opt. Express* **2012**, *20*, 24218–24225. [[CrossRef](#)] [[PubMed](#)]

107. Dudley, J.M.; Genty, G.; Coen, S. Supercontinuum generation in photonic crystal fiber. *Rev. Mod. Phys.* **2006**, *78*, 1135–1184. [[CrossRef](#)]
108. Al-kadry, A.; Baker, C.; El Amraoui, M.; Messaddeq, Y.; Rochette, M. Broadband supercontinuum generation in As₂Se₃ chalcogenide wires by avoiding the two-photon absorption effects. *Opt. Lett.* **2013**, *38*, 1185–1187. [[CrossRef](#)]
109. Rudy, C.W.; Marandi, A.; Vodopyanov, K.L.; Byer, R.L. Octave-spanning supercontinuum generation in in situ tapered As₂S₃ fiber pumped by a thulium-doped fiber laser. *Opt. Lett.* **2013**, *38*, 2865–2868. [[CrossRef](#)]
110. Sun, Y.A.; Dai, S.X.; Zhang, P.Q.; Wang, X.S.; Xu, Y.S.; Liu, Z.J.; Chen, F.F.; Wu, Y.A.; Zhang, Y.J.; Wang, R.P.; et al. Fabrication and characterization of multimaterial chalcogenide glass fiber tapers with high numerical apertures. *Opt. Express* **2015**, *23*, 23472–23483. [[CrossRef](#)]
111. Anashkina, E.A.; Shiryaev, V.S.; Koptev, M.Y.; Stepanov, B.S.; Muravyev, S.V. Development of of As-Se tapered suspended-core fibers for ultra-broadband mid-IR wavelength conversion. *J. Non-Cryst. Solids* **2018**, *480*, 43–50. [[CrossRef](#)]
112. Leonov, S.O.; Wang, Y.C.; Shiryaev, V.S.; Snopatin, G.E.; Stepanov, B.S.; Plotnichenko, V.G.; Vicentini, E.; Gambetta, A.; Coluccelli, N.; Svelto, C.; et al. Coherent mid-infrared supercontinuum generation in tapered suspended-core As₃₉Se₆₁ fibers pumped by a few-optical-cycle Cr:ZnSe laser. *Opt. Lett.* **2020**, *45*, 1346–1349. [[CrossRef](#)]
113. Leindecker, N.; Marandi, A.; Byer, R.L.; Vodopyanov, K.L. Broadband degenerate OPO for mid-infrared frequency comb generation. *Opt. Express* **2011**, *19*, 6304–6310. [[CrossRef](#)] [[PubMed](#)]
114. Reid, D.T.; Gale, B.J.S.; Sun, J. Frequency comb generation and carrier-envelope phase control in femtosecond optical parametric oscillators. *Laser Phys.* **2008**, *18*, 87–103. [[CrossRef](#)]
115. Keilmann, F.; Gohle, C.; Holzwarth, R. Time-domain mid-infrared frequency-comb spectrometer. *Opt. Lett.* **2004**, *29*, 1542–1544. [[CrossRef](#)]
116. Erny, C.; Moutzouris, K.; Biegert, J.; Kuhlke, D.; Adler, F.; Leitenstorfer, A.; Keller, U. Mid-infrared difference-frequency generation of ultrashort pulses tunable between 3.2 and 4.8 μm from a compact fiber source. *Opt. Lett.* **2007**, *32*, 1138–1140. [[CrossRef](#)]
117. Del’Haye, P.; Herr, T.; Gavartin, E.; Gorodetsky, M.L.; Holzwarth, R.; Kippenberg, T.J. Octave spanning tunable frequency comb from a microresonator. *Phys. Rev. Lett.* **2011**, *107*, 063901. [[CrossRef](#)] [[PubMed](#)]
118. Del’Haye, P.; Schliesser, A.; Arcizet, O.; Wilken, T.; Holzwarth, R.; Kippenberg, T.J. Optical frequency comb generation from a monolithic microresonator. *Nature* **2007**, *450*, 1214–1217. [[CrossRef](#)]
119. Bernhardt, B.; Sorokin, E.; Jacquet, P.; Thon, R.; Becker, T.; Sorokina, I.T.; Picque, N.; Hansch, T.W. Mid-infrared dual-comb spectroscopy with 2.4 μm Cr²⁺:ZnSe femtosecond lasers. *Appl. Phys. B* **2010**, *100*, 3–8. [[CrossRef](#)]
120. Adler, F.; Cossel, K.C.; Thorpe, M.J.; Hartl, I.; Fermann, M.E.; Ye, J. Phase-stabilized, 1.5 W frequency comb at 2.8–4.8 μm. *Opt. Lett.* **2009**, *34*, 1330–1332. [[CrossRef](#)] [[PubMed](#)]
121. Lee, K.F.; Granzow, N.; Schmidt, M.A.; Chang, W.; Wang, L.; Coulombier, Q.; Troles, J.; Leindecker, N.; Vodopyanov, K.L.; Schunemann, P.G.; et al. Midinfrared frequency combs from coherent supercontinuum in chalcogenide and optical parametric oscillation. *Opt. Lett.* **2014**, *39*, 2056–2059. [[CrossRef](#)] [[PubMed](#)]
122. Sanghera, J.S.; Shaw, L.B.; Busse, L.E.; Talley, D.; Aggarwal, I.D. Infrared transmitting fiber optics for biomedical applications. In Proceedings of the BiOS ’99 International Biomedical Optics Symposium, San Jose, CA, USA, 23–29 January 1999; Volume 3596, pp. 178–187.
123. Sanghera, J.S.; Kung, F.H.; Busse, L.E.; Pureza, P.C.; Aggarwal, I.D. Infrared evanescent absorption-spectroscopy of toxic-chemicals using chalcogenide class fibers. *J. Am. Ceram. Soc.* **1995**, *78*, 2198–2202. [[CrossRef](#)]
124. Michel, K.; Bureau, B.; Pouvreau, C.; Sangleboeuf, J.C.; Boussard-Pledel, C.; Jouan, T.; Rouxel, T.; Adam, J.L.; Staubmann, K.; Steinner, H.; et al. Development of a chalcogenide glass fiber device for in situ pollutant detection. *J. Non-Cryst. Solids* **2003**, *326*, 434–438. [[CrossRef](#)]
125. Huang, P.; Huang, T.Y.; Zeng, S.W.; Pan, J.X.; Wu, X.; Zhao, X.; Wu, Y.H.; Ping, P.S.; Brambilla, G. Nonlinear gas sensing based on third-harmonic generation in cascaded chalcogenide microfibers. *J. Opt. Soc. Am. B* **2019**, *36*, 300–305. [[CrossRef](#)]
126. Wang, J.Q.; Chen, Y.Z.; Geng, Y.F.; Hong, X.M.; Li, X.J. Theoretical design of mid-infrared graphene optical gas sensor based on slot Si core fiber. *IEEE Photonics Technol. Lett.* **2019**, *31*, 1096–1099. [[CrossRef](#)]
127. Wang, M.; Yang, F.; Dai, S.X.; Cao, Z.F.; Su, J.X.; Ding, S.J.; Zhang, P.Q. Effect of the geometries of Ge-Sb-Se chalcogenide glass tapered fiber on the sensitivity of evanescent wave sensors. *J. Lightwave Technol.* **2021**, *39*, 4828–4836. [[CrossRef](#)]
128. Michel, K.; Bureau, B.; Boussard-Pledel, C.; Jouan, T.; Adam, J.L.; Staubmann, K.; Baumann, T. Monitoring of pollutant in waste water by infrared spectroscopy using chalcogenide glass optical fibers. *Sens. Actuators B Chem.* **2004**, *101*, 252–259. [[CrossRef](#)]
129. Keirsse, J.; Boussard-Pledel, C.; Loreal, O.; Sire, O.; Bureau, B.; Turlin, B.; Leroyer, P.; Lucas, J. Chalcogenide glass fibers used as biosensors. *J. Non-Cryst. Solids* **2003**, *326*, 430–433. [[CrossRef](#)]
130. Le Coq, D.; Michel, K.; Keirsse, J.; Boussard-Pledel, C.; Fonteneau, G.; Bureau, B.; Le Quere, J.M.; Sire, O.; Lucas, J. Infrared glass fibers for in-situ sensing, chemical and biochemical reactions. *Comptes Rendus Chim.* **2002**, *5*, 907–913. [[CrossRef](#)]
131. Hocde, S.; Loreal, O.; Sire, O.; Boussard-Pledel, C.; Bureau, B.; Turlin, B.; Keirsse, J.; Leroyer, P.; Lucas, J. Metabolic imaging of tissues by infrared fiber-optic spectroscopy: An efficient tool for medical diagnosis. *J. Biomed. Opt.* **2004**, *9*, 404–407. [[CrossRef](#)] [[PubMed](#)]

-
132. Gutierrez-Arroyo, A.; Baudet, E.; Bodiou, L.; Nazabal, V.; Rinnert, E.; Michel, K.; Bureau, B.; Colas, F.; Charrier, J. Theoretical study of an evanescent optical integrated sensor for multipurpose detection of gases and liquids in the mid-infrared. *Sens. Actuators B Chem.* **2017**, *242*, 842–848. [[CrossRef](#)]
 133. Wang, X.M.; Su, J.X.; Wang, Y.Y.; Yang, C.F.; Dai, S.X.; Zhang, P.Q. High-sensitivity sensing in bare Ge-Sb-Se chalcogenide tapered fiber with optimal structure parameters. *J. Non-Cryst. Solids* **2021**, *559*, 120686. [[CrossRef](#)]